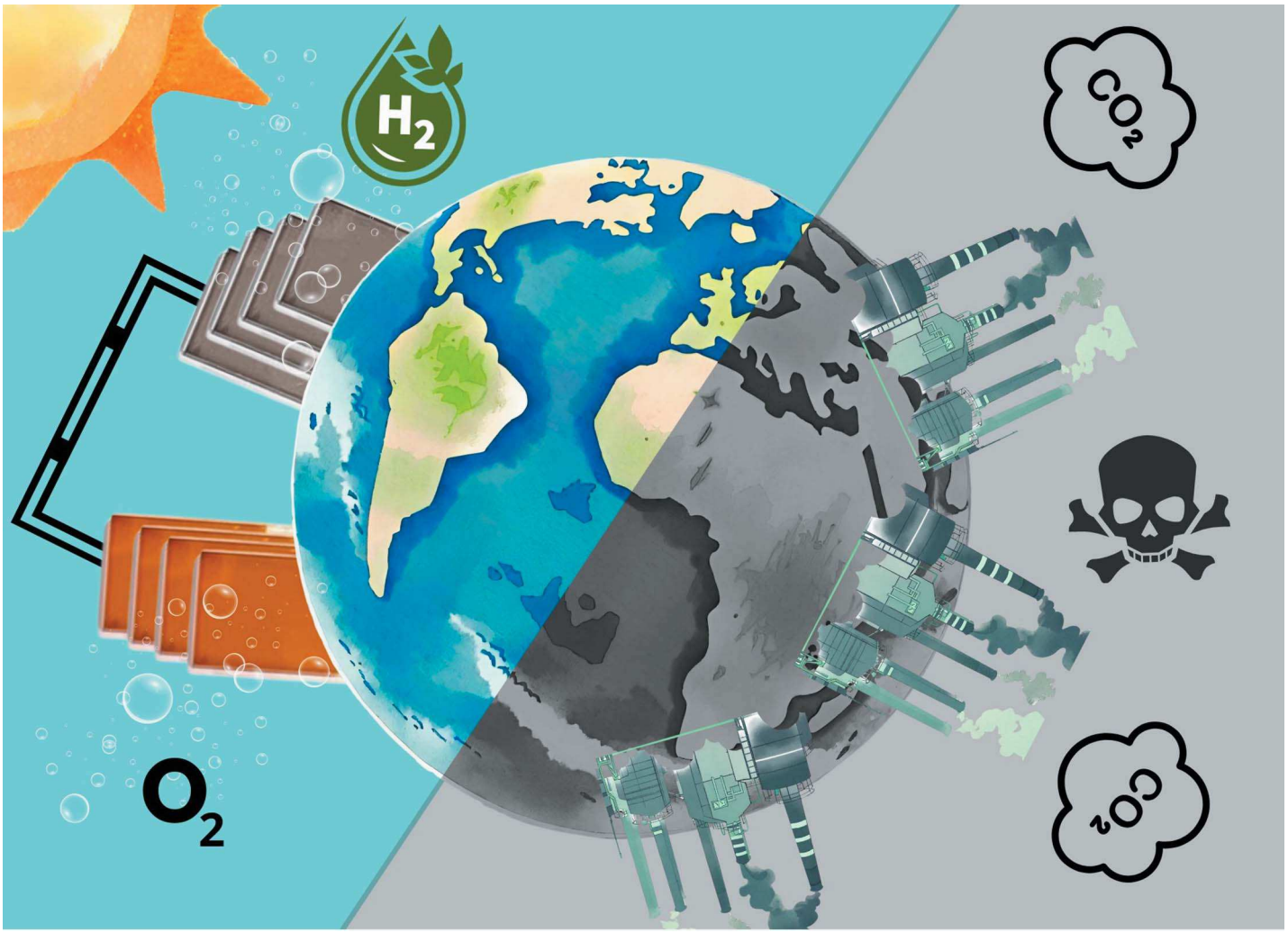

Featuring a study on hematite photoanodes engineered by a polymeric precursor solution method carried out by a group of researchers led by Dr Flavio L. Souza at the Brazilian Nanotechnology National Laboratory.

Dual modification on hematite to minimize small polaron effects and charge recombination for sustainable solar water splitting

A novel synthetic strategy was developed to leverage earth-abundant Al^{3+} and Zr^{4+} in a dual-chemical modification to synergistically minimize small polaron effects and interfacial charge recombination on hematite nanostructure. The polymer precursor solution method simultaneously induces Al^{3+} doping of hematite crystal lattice while Zr^{4+} forms interfacial excess, creating a single-phased homogenous nanostructured thin film. The engineered photoanode increased solar conversion efficiency by 6.5 times when compared to pristine hematite.

As featured in:

See Flavio L. Souza *et al.*, *J. Mater. Chem. A*, 2024, **12**, 6280.

ROYAL SOCIETY OF CHEMISTRY

rsc.li/materials-a

Registered charity number: 207890

Journal of Materials Chemistry A

ROYAL SOCIETY OF CHEMISTRY

PAPER

View Article Online
View Journal | View Issue

Cite this: J. Mater. Chem. A, 2024, 12, 6280

Dual modification on hematite to minimize small polaron effects and charge recombination for sustainable solar water splitting†

Nathália C. Verissimo,‡[a] Fabio A. Pires,‡[ab] Ingrid Rodríguez-Gutiérrez,[ac] Jefferson Bettini,[a] Tanna E. R. Fiuza,[a] Cleyton A. Biffe,[a] Fabiano E. Montoro,[a] Gabriel R. Schleder,[ad] Ricardo H. R. Castro,[ae] Edson R. Leite[af] and Flavio L. Souza *[abc]

Hematite nanostructures are strong candidates for the development of sustainable water splitting technologies. However, major challenges exist in improving charge density and minimizing charge recombination rates for a competitive photoelectrochemical performance based on hematite without compromising sustainability aspects. Here we develop a synthetic strategy to leverage earth-abundant Al^{3+} and Zr^{4+} in a dual-chemical modification to synergistically minimize small polaron effects and interfacial charge recombination. The solution-based method simultaneously induces Al^{3+} doping of the hematite crystal lattice while Zr^{4+} forms interfacial excess, creating a single-phased homogeneous nanostructured thin film. The engineered photoanode increased photocurrent from 0.7 mA cm^{-2} for pristine hematite up to 4.5 mA cm^{-2} at 1.23 V and beyond 6.0 mA cm^{-2} when applying an overpotential of 300 mV under simulated sunlight illumination (100 mW cm^{-2}). The results demonstrate the potential of dual-modification design using solution-based processes to enable sustainable energy technologies.

Received 13th December 2023
Accepted 19th January 2024

DOI: 10.1039/d3ta07721g

rsc.li/materials-a

1 Introduction

Hematite (α-Fe_2O_3) has a relatively small electronic band gap (1.9–2.1 eV) which allows for a theoretical 17% solar-to-hydrogen efficiency in photoelectrochemical devices, and a maximum photocurrent of 14 mA cm^{-2}.[1] Owing to this potential and hematite's inherent low toxicity and environmental appeal, several techniques have been reported for the synthesis of hematite photoanodes for solar water-splitting.[2] However, conventional manufacturing strategies lead to undesirable microstructures with high concentrations of recombination sites in hematite photoanodes, causing poor hole diffusion length and limiting the lifetime of electron–hole pairs, which negatively impacts on the device's efficiencies.[3] Hydrothermal, solvothermal, and colloidal methods have demonstrated potential to produce columnar morphologies of hematite that mitigate some microstructural drawbacks with relative success.[4,5] Alternatively, polymeric precursor methods offer significant processing benefits over hydrothermal processes for a more economically competitive alternative with greater potential for scaling up. However, these solution-based methods bring their own microstructural challenges, primarily associated with the extensive interfacial network acting as trapping states for electrons and holes alike.[6]

Polymeric precursor solution (PPS) synthesis refers to preparing polycrystalline oxide thin films by depositing a polymer solution on a substrate *via*, *e.g.*, spin, dip, or spray-coating techniques. While the method is proven suitable for industrial applications, the produced films are typically composed of several interfaces, including grain–grain, grain-liquid, and grain-substrate, all significantly influencing the charge dynamics by acting as electron–hole recombination sites. Several studies have attempted to optimize PPS and surpass the

[a]Brazilian Nanotechnology National Laboratory (LNNano), Brazilian Center for Research in Energy and Materials (CNPEM) – Campinas, SP, Brazil. E-mail: flavio.souza@lnnano.cnpem.br

[b]Institute of Chemistry, State University of Campinas (UNICAMP) – Campinas, SP, Brazil

[c]Center for Natural and Human Sciences, Federal University of ABC (UFABC) – Santo André, SP, Brazil

[d]John A. Paulson School of Engineering and Applied Sciences, Harvard University, Cambridge, MA, 02138, USA

[e]Department of Materials Science and Engineering, Lehigh University, Bethlehem, Pennsylvania, USA

[f]Departamento de Química, Universidade Federal de São Carlos, 13565-905, Brazil

† Electronic supplementary information (ESI) available: Description of characterization methods and data analysis; current–potential (*J–V*) curves under simulated light conditions (100 mW cm^{-2}) in 1 M NaOH with and without H_2O_2 as a hole scavenger; transmission coefficient curves of DFT calculations; IMPS model employed and plots; onset potentials calculated from d*J*/d*V* curves; XPS results of studied samples before and after PEC operation; cyclic voltammograms; open circuit potential measurements; electrochemical impedance spectroscopy (EIS) calculations and Nyquist plots; UPS spectra; Tauc plots; schematic band diagrams. See DOI: https://doi.org/10.1039/d3ta07721g

‡ These authors contributed equally to this work.

interfacial issues, with significant successes building on: (a) a better understanding of the impact of annealing temperature on the photoanode activity;[7] (b) the design of improved wettability by solvent exchange[8] or solvent mixture;[9] and most importantly (c) the fundamental understanding of the relationship between the dopant location in the system and hematite photoelectrochemical (PEC) performance.[10]

Doping to improve carrier conductivity of hematite acts in two complementary mechanisms, the formation of a solid solution impacting intrinsic crystal lattice defects or the formation interface excess, *i.e.*, local concentration enrichment, which impacts interfacial defects. In metal oxides, the charge carrier can locally deform the lattice due to the carrier-phonon coupling, inducing a potential dwell that acts as a carrier trap called a small polaron.[11] Solid solution dopants with stronger correlated electrons than the 3d electrons of Fe are potential candidates for minimizing polaron effects, but their effects are limited in concentration by the formation of multipole clusters.[12] At the same time, polycrystalline structures, such as those derived from the polymeric precursor, show a greater magnitude of isolated electron polaron adsorption, implying a key role of interface defects in the carrier conduction. Those need to be addressed by dopants prone to form interfacial excess, acting, for example, on the local energy barriers[13] between grains or even at the grain-substrate interfaces.[10]

Recently, Pires *et al.* explored the possibility of concomitantly manipulating the crystalline lattice and interfaces in a single precursor solution.[14] Dual modification of oxides has been reported focusing on the synergistic influence of ions with mixed valence states.[15–26] However, the PPS synthesis strategy can be used to specifically favor dopant solid-solution or dopant interfacial segregation by manipulating the chemistry of a polymeric solution. In summary, the process entails the synthesis of a hematite polymeric precursor containing Fe^{3+} ions mixed with the ion designed to form a thermodynamic solid solution. This polymer is concentrated and thoroughly polymerizes into a thermoplastic gel. The ion selected to segregate is then solubilized in ethanol and mixed with that polymer gel. This causes the additional dopant to pervade around the polymer clusters, inducing interface enrichment during the annealing process. Pires *et al.* demonstrated an improvement in PEC performance by using Ga^{3+} as a lattice dopant and Hf^{4+} as an interfacial dopant.[14] Although they achieved a sevenfold increase in photocurrent in comparison to pristine hematite, here we draw the hypothesis that a knowledgeable selection of the dopants for both the crystalline lattice and interfaces can yield a more significant performance improvement by thoroughly exploring the novel synthetic protocol while also considering sustainability matters.

Based on this, we hypothesize that a designed dual modification of hematite using earth abundant elements Al^{3+} and Zr^{4+} as crystal lattice and interface doping agents, respectively, would improve the overall performance of the photoanode for solar water splitting and achieve benchmark photocurrent values. Al_2O_3 is isostructural to hematite, crystallizing in the corundum structure with lattice parameters $a = b = 4.76$ Å and $c = 12.989$ Å,[27] in contrast to hematite with $a = b = 5.03$ Å and $c = 13.74$ Å.[28] The more compact structure of Al_2O_3 is a result of the greater ionic character of the bonds given the smaller ionic radius of Al^{3+}. While the Al_2O_3–Fe_2O_3 phase diagram predicts significant solid solution in both aluminum and iron rich sides at elevated temperatures (~1000 °C), at lower temperatures the solubility limit of Al^{3+} into hematite reduces, but data at room temperature is hardly available. First-principles DFT calculations show Al^{3+} substitutes Fe^{3+} ions giving a more ionic character to the bonds with oxygen, causing minor changes in the local energy levels.[29] Hence, Al^{3+} induces a local negative strain in its surrounding lattice due to the shorter bonds with oxygen,[30] which associated with its stable valence state induces conductivity increase by impacting polaron migration.[31]

The dissimilarities between Zr^{4+} and Fe^{3+} ions, however, suggest unfavorable formation of a solid solution. While Launay and Horowitz[32] reported the positive impact of zirconium addition on α-Fe_2O_3 single crystals for PEC, Simfukwe *et al.*[33] documented highly favorable formation energies for Zr^{4+} positioned near the α-Fe_2O_3 interface region by DFT. Zr^{4+} causes the conduction band minimum to be delocalized for a potentially improved carrier mobility.[34] In fact, Zr^{4+} segregation to interfaces is experimentally observed in other corundum structures[35] and even in nanoscaled spinel Al_2O_3,[36] where it causes a measurable reduction of surface excess energy for improved crystal stability. Bedin *et al.* also explored the impact of Zr^{4+} as a single dopant in hematite revealing a significant photocurrent increase associated with the predicted segregation of Zr^{4+} to both grain–grain and grain-substrate interfaces.[9]

Therefore, here we explore the PPS synthesis method to introduce both Al^{3+} and Zr^{4+} into hematite nanostructures particularly targeting the selective allocation of Al^{3+} within the crystal lattice and Zr^{4+} at the interfaces to synergistically address the local issues limiting hematite performance. The method formulates a single chemical solution which delivers refined control over the microstructure of the thin films in terms of thickness, roughness, and wetting, while enabling an unprecedented control of dopant positioning as confirmed by elemental chemical mapping. The synergistic effect of these earth abundant dopants caused an increase in photocurrent from 0.7 mA cm^{-2} for pristine hematite up to 4.5 at 1.23 V *versus* the reversible hydrogen electrode (RHE), with photocurrents beyond 6.0 mA cm^{-2} at 1.5 V_{RHE} when tested under simulated sunlight illumination (100 mW cm^{-2}) in 1 M NaOH electrolyte using the co-catalyst $NiFeO_x$. The results establish not only the potential of this novel chemical strategy to atomically engineer thin films, but also demonstrate the impact of atomic-level engineering on device performance.

2 Experimental procedures

2.1 Production of hematite-based photoanodes

The main processes and conditions employed in the production of hematite-based thin films by the polymeric precursor (PPS) method are summarized in Fig. 1. Detailed information of each step is provided in the following sections: "Substrate cleaning", "Precursor solution preparation", "Film deposition", and "Thermal treatments".

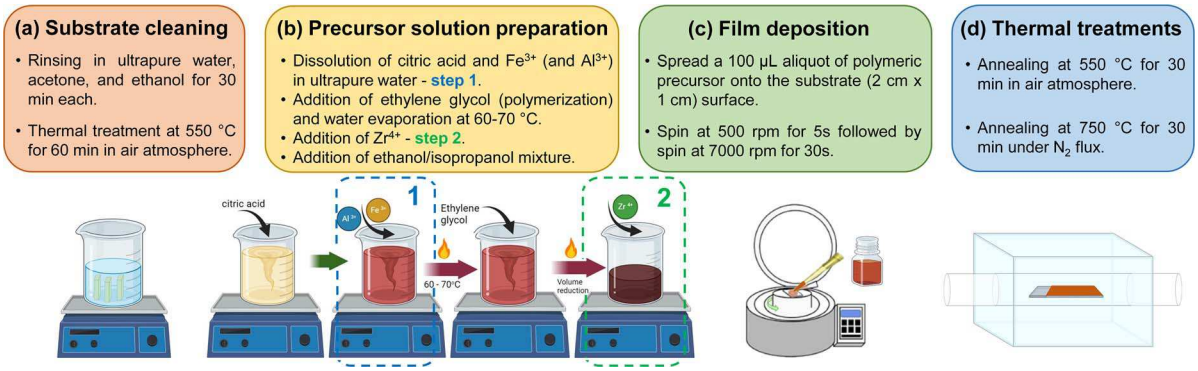

Fig. 1 Step-by-step production of hematite-based thin films by the polymeric precursor solution (PPS) method. Substrate cleaning (a), precursor solution preparation (b), film deposition (c), and thermal treatments (d) are the main processes. Highlighted dashed boxes in the precursor solution preparation (b) show the designed addition of Al^{3+} before polymer formation (1) and Zr^{4+} addition after polymer formation (2).

2.1.1 Substrate cleaning. Prior to the deposition of the thin films, aluminum borosilicate glass coated with F:SnO_2 substrates (FTO, Solaronix, resistivity of 8–10 Ω cm, >80% transmission from 500 to 800 nm) were cleaned by successive rinsing in Milli-Q water (18.2 MΩ cm), acetone and ethanol for 30 min at 90 °C, 60 °C, and 70 °C, respectively, for 30 min each (Fig. 1a). In sequence, the substrates were thermally treated at 550 °C for 60 min in a horizontal tube furnace (Lindberg/Blue M Mini-Mite).

2.1.2 Precursor solution preparation. Pristine and modified hematite precursors were prepared following the synthesis method shown in Fig. 1b. For the Al–Zr-modified precursor, 5.88 g of citric acid (J.T. Baker, 99.5%) was dissolved into 10.0 mL of Milli-Q water (18.2 MΩ cm, 25 °C) in a 50 mL vessel under continuous stirring for 10 minutes. Then, 5.18 g of $Fe(NO_3)_3 \cdot 9H_2O$ (Alfa Aesar, 99.5%) and 250 µL of $Al(NO_3)_3 \cdot 9H_2O$ (Sigma-Aldrich, 99%) aqueous solution were added to the system, obtaining a final concentration of 0.5% Al^{3+}, in the Al^{3+} : Fe^{3+} molar ratio, as highlighted in the dashed blue box (1) of Fig. 1b. The system was then heated up to 60–70 °C and 2.5 mL of ethylene glycol (Sigma-Aldrich, 99.8%) was added to the mixture, which was kept under heating and stirring until it reached 50% of its initial volume. At this point, an aliquot of 500 µL of 1.0% ethanol solution of $ZrO(NO_3)_2 \cdot xH_2O$ (Alfa-Aesar, 99.9%) was added to the polymeric precursor to obtain a final concentration of 3.0% Zr^{4+} (Zr^{4+} : Fe^{3+} molar ratio), as highlighted in the dashed green box (2) of Fig. 1b. Finally, an alcohol mixture of 1.50 mL of anhydrous ethanol (Synth, 99.8%) and 1.00 mL of isopropyl alcohol (Synth, 99.5%) was added to 5.0 mL of the obtained precursor solution. Reference solutions were also prepared to produce pristine hematite (H), Al-doped hematite (H-Al) and Zr-modified hematite (H-Zr) precursors.

2.1.3 Film deposition. Aliquots of 100.0 µL of the polymeric solutions were spin-coated onto the FTO surface at 500 rpm for 5 s followed by 7000 rpm for 30 s (Fig. 1c). The as-deposited films were then placed into a hot plate for 5 minutes at 90 °C.

2.1.4 Thermal treatments. After the deposition, the films were annealed at 550 °C in an air atmosphere for 30 min (Lindberg/Blue M Mini-Mite horizontal tube furnace) and subsequentially at 750 °C under N_2 flux (150 mL min^{-1}) for 30 min in a tube furnace with automatic sliding quartz (MTI Corporation, model OTF-1200X-50-SL), as shown in Fig. 1d. The regions where the films were placed for annealing had their temperatures verified with an external thermocouple.

2.2 Structural, optical, and morphological characterization

X-ray photoelectron spectroscopy (XPS) was performed in a Thermo Scientific K-alpha device with a monochromatic Al Kα radiation ($\lambda = 1.48$ Å) excitation source. Ultraviolet photoelectron spectroscopy (UPS) measurements were carried out in a Specs XPS/UPS system with a Phoibos 150 analyzer and a CMOS 2D detector using a He I line (21.22 eV) from a UHV gas discharge lamp. The acceleration potential of −4 V was applied to the samples. Optical measurements were performed in a Shimadzu UV-VISNIR spectrophotometer UV-3600 Plus equipped with an integrating sphere. Absorption spectra were recorded from 240 to 800 nm. Kelvin probe force microscopy (KPFM) measurements were performed in an NX-10 Park Systems microscope, with a NanoSensorsTM Pt/Ir-coated silicon probe, model PPP-EFM. Scanning image areas of 1 mm × 1 mm with a resolution of 512 × 512 pixels were recorded. Focused-ion beam scanning electron microscopy (FIB-SEM) images were acquired with a Quanta FEG 650 microscope from FEI Company, with a T2 detector. Scanning transmission electron microscopy (STEM) analysis was performed in a JEOL JEM 2100F microscope equipped with energy dispersive X-ray spectroscopy (EDS) module Oxford SDD X-Max 80 mm^2. EDS data was acquired simultaneously to STEM using a 0.7 nm probe size and a 0.3 s acquisition time. The elemental and atomic concentration maps were obtained using the Gatan GMS plugin.

2.3 Electrochemical characterization

The photoanodes were assembled in a three-electrode electrochemical cell containing a platinum counter electrode and a commercial (Metrohm Autolab) Ag/AgCl(sat) reference electrode. A saturated calomel electrode (SCE) was also employed as a reference electrode for linear sweep voltammetry (LSV) measurements. The hematite-based photoanodes were used as

working electrodes (0.196 cm^2) in 1.0 M NaOH (Sigma-Aldrich, 98%) and 1 M NaOH + 0.5 M H_2O_2 electrolyte solutions (pH = 13.6). Using a potentiostat/galvanostat (Autolab PGSTAT 302N), linear sweep voltammetry (LSV) measurements were conducted under sunlight illumination (100 mW cm^{-2}) simulated by a 450 W Xe lamp (Osram, ozone free) equipped with an AM 1.5 Global filter at a scan rate of 50 mV s^{-1}. The power (1 sun) was adjusted and calibrated to the position of the photoanodes with the aid of an optical-meter (Newport 843-R-USB). In the same electrochemical setup, open circuit potential (OCP) measurements were performed during 900 s with 0.5 s interval time, under dark conditions for 300 s, illumination for the subsequent 300 s, and interruption of illumination for 300 s. Electrochemical impedance spectroscopy (EIS) measurements were performed under dark conditions with a Frequency Response Analyzer (FRA32M) module. Mott–Schottky data was extracted from 0.25 V to 1.75 V at 1 kHz frequency and analyzed at the linear region of the curves. EIS experiments were also conducted under 100 mW cm^{-2} simulated solar illumination at 1.23 V *vs.* RHE and the equivalent circuit modelling was obtained by fitting Nyquist plots with the Zview software. Chronoamperometry experiments at 1.23 V *vs.* the reversible hydrogen electrode (RHE) were carried out for 5 h with 1 s interval time under 100 mW cm^{-2} illumination concomitantly with gas chromatography (GC System 7890B Agilent Technologies equipped with a thermal conductivity detector – TCD) in a three-electrode cell configuration for quantification of gaseous products. Incident photon-to-current efficiency (IPCE) measurements at 1.23 V *vs.* RHE were conducted with a Metrohm μAUTOLAB 3 electrochemical impedance analyzer and a Newport/Oriel 74 125 Cornerstone 260 UV-vis 1/4 m monochromator. Intensity modulated photocurrent spectroscopy (IMPS) analysis was performed using the FRA32M module coupled with a LED driver. A monochromatic blue LED (470 nm) was used to generate a sinusoidal oscillating light intensity in a frequency range from 20 kHz to 0.1 Hz under calibrated 30 mW cm^{-2} illumination. The amplitude of the modulation was set at 10% of the base light intensity. All potentials from electrochemical characterizations were converted to the reversible hydrogen electrode (RHE) scale using the Nernst equation.

3 Results and discussion

Hematite-based photoanodes were produced by spin-coating a polymeric precursor solution onto FTO substrates, followed by thermal treatments. A rigorous cleaning process of the commercial FTO substrates prior to deposition (Fig. 1a) was adopted due to the resizing of the as-received slides to 2 cm^2 samples, with subsequent thermal treatment to remove impurities that could impact the substrate conductivity. The pristine hematite (H) polymeric precursor was prepared by mixing Fe^{3+} ions in citric acid and ethylene glycol solution. This mixture was heated to cause polyesterification and enable cations to chelate through the polyester. For the Al^{3+} doped precursor (H-Al), aiming at favoring the solid solution with Fe^{3+} in the hematite structure, the cations were mixed with Fe^{3+} before the polymerization into the gel, enabling a homogeneous distribution of both ions in the liquid phase (dashed blue box in Fig. 1b). For Zr^{4+} addition, the previously produced gel containing Fe^{3+} or Al^{3+}/Fe^{3+} was reduced to 50% of its volume by slow evaporation and, only after the precursor concentration, a Zr^{4+} solution in ethanol was poured into the thermoplastic gel to produce the so-called H-Zr and H-Al–Zr gels (dashed green box in Fig. 1b). The protocol (detailed in Fig. 1b from the Experimental section) was chosen for Al^{3+} and Zr^{4+} to have different chemical environments in the polymeric precursor, potentially favoring Al^{3+} to dope the hematite lattice and Zr^{4+} to segregate at the interfaces. It is important to highlight that the stoichiometric addition of reagents maintaining the proportions of solvent, citric acid, ethylene glycol, and metal salts was engineered to keep the total solid amount constant in the precursors.

After spin-coating deposition (Fig. 1c), in which the same procedure was employed for all samples to allow homogeneous and reproducible deposits (500 rpm for 5 s and 7000 rpm for 30 s), the samples were annealed at 550 °C for 30 min in an air atmosphere to remove organic compounds and promote hematite phase formation, and then placed at 750 °C for 30 min under controlled N_2 flux to activate the film surface for photoelectrochemical application (Fig. 1d). As part of the synthesis design, the optimal Al^{3+} and Zr^{4+} concentrations were evaluated based on their photocurrent response under sunlight illumination at 100 mW cm^{-2} (Fig. S1†). Both cations showed a photocurrent increase as a function of concentration followed by a decrease, likely attributed to multipole clustering.[12] The maximum photocurrents were obtained for the samples containing 0.5% Al^{3+} (named H-0.5Al) and 3.0% Zr^{4+} (named H-3.0Zr), and therefore those concentrations were used to design the dual-modified photoanode (named H-0.5Al–3.0Zr).

For a direct comparison and to highlight the impact of the dual modification in contrast to the individual doping, linear voltammetry measurements were performed for H, H-0.5Al, H-3.0Zr, and H-0.5Al–3.0Zr to evaluate the photocurrent response under simulated AM 1.5G sunlight (100 mW cm^{-2}), as outlined in Fig. 2a. The photocurrent response in the dark was negligible due to its low catalytic behavior. Under illumination, H and H-Al photoanodes exhibited a photocurrent response at 1.23 V *versus* the reversible hydrogen electrode (RHE) of 0.7 mA cm^{-2} and 1.35 mA cm^{-2}, respectively. The H-Zr achieved a value of 1.95 mA cm^{-2}, and the dual-modified H-Al–Zr photoanode led to a maximum photocurrent response of 3.5 mA cm^{-2} at 1.23 V_{RHE} and up to 5.0 mA cm^{-2} at 1.5 V_{RHE}. To further improve the photoelectrochemical performance of the photoanodes, a commonly known co-catalyst, $NiFeO_x$, was electrodeposited[37] onto the H-Al–Zr sample, leading to a photocurrent enhancement to 4.5 mA cm^{-2} at 1.23 V_{RHE} and up to values beyond 6.0 mA cm^{-2} at 1.5 V_{RHE} (Fig. 2a). Following the protocol in which the precursors have the same total solid amount and were deposited following the same spin-coating conditions, homogeneous thin films (Fig. S2a†) and reproducible H-0.5Al–3.0Zr/$NiFeO_x$ photoanodes (Fig. S2b†) were obtained. Moreover, Fig. S3† show the photoresponses were maintained when using a saturated calomel electrode (SCE) as the reference electrode, indicating Ag/AgCl instability in alkaline media was negligible in these measurements.

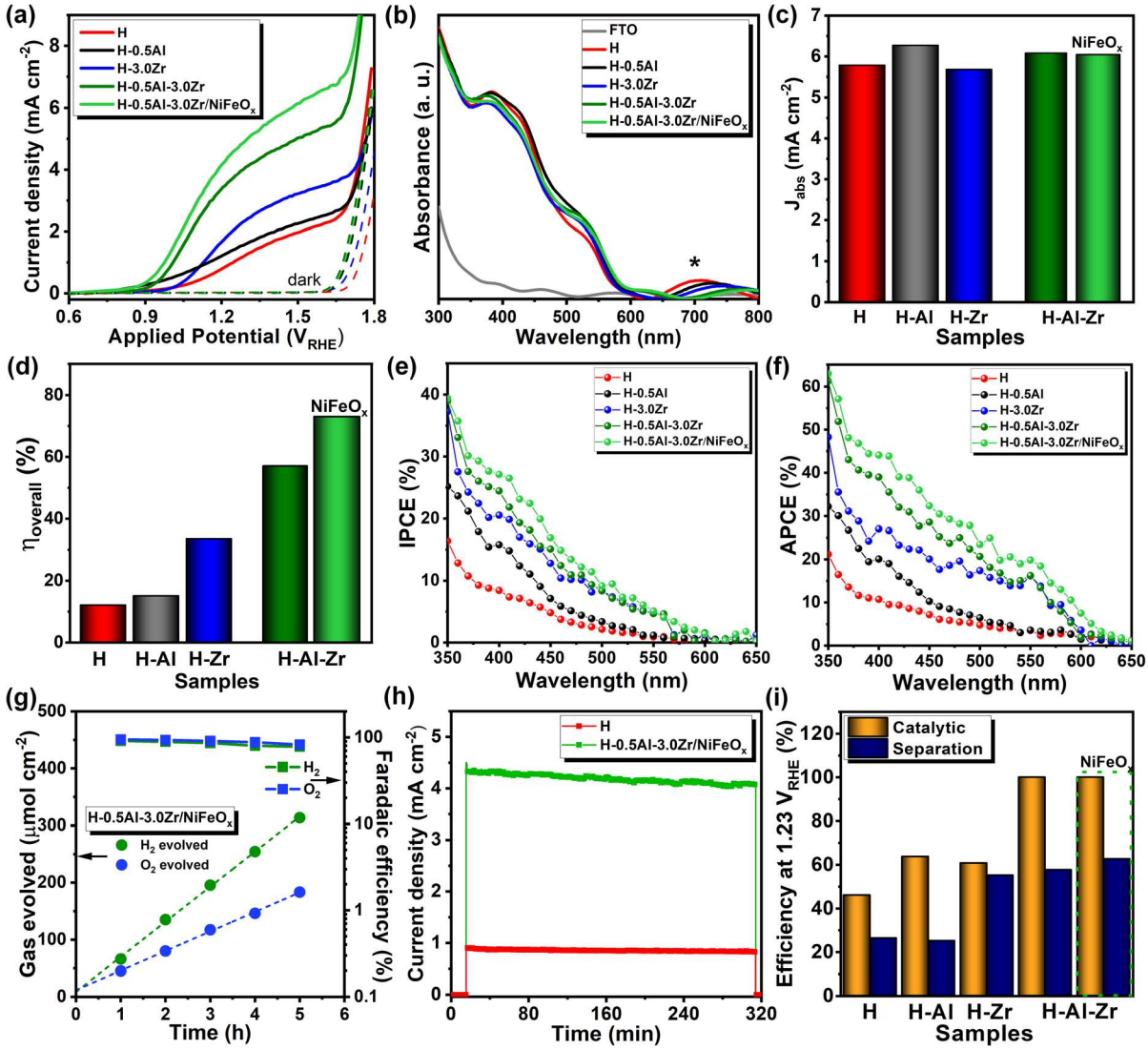

Fig. 2 (a) Linear sweep voltammetry measurements (*j*, *V* curves) of the photoanodes under AM 1.5G 100 mW cm^{-2} illumination in 1 M NaOH electrolyte. (b) Absorbance profiles of the FTO substrate and the photoanodes in the visible range of the electromagnetic spectrum. Light absorption highlighted (*) with $\lambda > 600$ nm corresponds to an Urbach tail, which is attributed to light absorption by the shallow trapping states of hematite. (c) Maximum current values determined by the absorption properties of the photoanodes (J_{abs}) calculated in the visible range of the electromagnetic spectrum. (d) Overall photoanode efficiency ($\eta_{overall}$) representing the total yield of current photogenerated in relation to the maximum current permitted by the absorption properties (J_{abs}) of pristine hematite (H), H-0.5Al, H-3.0Zr, H-0.5Al–3.0Zr, and H-0.5Al–3.0Zr/NiFeO$_x$. (e) Incident photon-to-current efficiency (IPCE) of H, H-0.5Al, H-3.0Zr, H-0.5Al–3.0Zr, and H-0.5Al–3.0Zr/NiFeO$_x$ at 1.23 V *vs.* the reversible hydrogen electrode (RHE) under AM 1.5G 100 mW cm^{-2} illumination in 1 M NaOH electrolyte. (f) Absorbed photon-to-current efficiency (APCE) of H, H-0.5Al, H-3.0Zr, H-0.5Al–3.0Zr, and H-0.5Al–3.0Zr/NiFeO$_x$ at 1.23 V *vs.* RHE under AM 1.5G 100 mW cm^{-2} illumination in 1 M NaOH electrolyte. (g) Amount of H_2 and O_2 evolved from photoelectrochemical operation of the H-0.5Al–3.0Zr/NiFeO$_x$ photoanode at 1.23 V *vs.* RHE under AM 1.5G 100 mW cm^{-2} illumination in 1 M NaOH electrolyte, and the faradaic efficiency of gas production during 5 h of measurements. (h) Chronoamperometry measurements of pristine hematite (H) and H-0.5Al–3.0Zr/NiFeO$_x$ at 1.23 V *vs.* RHE under AM 1.5G 100 mW cm^{-2} illumination in 1 M NaOH electrolyte. H-0.5Al–3.0Zr/NiFeO$_x$ *j*, *t* measurement was performed during gas quantification. (i) Catalytic efficiency ($\eta_{cat.}$) and charge separation efficiency ($\eta_{sep.}$) calculated for H, H-0.5Al, H-3.0Zr, H-0.5Al–3.0Zr, and H-0.5Al–3.0Zr/NiFeO$_x$ at 1.23 V *vs.* the reversible hydrogen electrode (RHE) under AM 1.5G 100 mW cm^{-2} illumination in 1 M NaOH + 0.5 M H_2O_2 electrolyte.

The addition of dopants did not significantly change the optical properties of hematite, as suggested by the absorbance profiles shown in Fig. 2b. Interestingly, the hematite-based materials produced following the PPS protocol showed light absorption at wavelengths higher than 600 nm. The absorptance calculated for the FTO substrate and pristine hematite (see Fig. S4†) shows these bands indeed correspond to absorbed light and therefore can be attributed to light absorption by shallow trapping states, which produces the characteristic Urbach tail observed. These defects cause spatial confinement in nanomaterials and suppression of phonon interactions, decreasing the probability of indirect transitions that will generate electric current.[38,39]

The similar optical properties observed for all photoanodes resulted in close values of maximum experimental currents from the absorption properties (J_{abs}) (Fig. 2c). Therefore, the half-cell overall efficiency ($\eta_{overall}$), which represents the total yield of current generated in relation to the J_{abs}, varied according to the dopant(s) introduced (Fig. 2d). The synergistic combination of Al^{3+} and Zr^{4+} incorporation (H-0.5Al–3.0Zr) delivered a photoanode with 57% of $\eta_{overall}$, and the addition of the $NiFeO_x$ co-catalyst enhanced the overall photoanode efficiency up to 73%, indicating a successful optimization that led to materials capable of achieving both cost-effective photocurrent generation and efficient sunlight to current conversion. Indeed, Fig. 2e shows a 2.5-fold increase in the incident photon-to-current efficiency (IPCE) values for H-0.5Al–3.0Zr/$NiFeO_x$ compared to pristine hematite at 350 nm, and 63% of absorbed photon-to-current efficiency (APCE) at the same wavelength (Fig. 2f), with spectral signature due to Al–Zr/$NiFeO_x$ modifications. Despite the observed light absorption at wavelengths beyond 600 nm, IPCE analysis shows that this absorption does not contribute to current generation, reinforcing that the defects are most likely absorbing light at wavelengths higher than 600 nm.

The high efficiencies translate into high faradaic efficiency of gas evolution, confirmed by the chromatographic gas quantification (Fig. 2g), which indicates that almost all photogenerated charge is used for the overall water splitting reaction. Moreover, chronoamperometry analysis (Fig. 2h) employed for faradaic efficiency calculations highlights the photoelectrochemical stability of the optimized H-Al–Zr/$NiFeO_x$ photoanode. Photocurrent variations as a function of time are associated with the experimental configuration used for the measurement, in which there is not a flowing feed of electrolyte to the system. This leaves the three-electrode cell susceptible to the agglomeration of bubbles over the photoanode measured area that affect the photoelectrochemical performance by scattering incident light. The H-Al–Zr/$NiFeO_x$ curve in Fig. 2h shows the effect of bubbles only after several minutes of operation. This is not an uncommon effect, and the "up and down" behavior has been attributed to nucleation, agglomeration, and then release of bubbles, as shown in Fig. S5.†[40] In general, this result implies the modifications introduced did not damage the α-Fe_2O_3 phase, corroborating its well-known stability,[41] but further analysis is required.

Furthermore, the comparative bar graph (Fig. 2i) shows the catalytic efficiency ($\eta_{cat.}$) and charge separation efficiency ($\eta_{sep.}$) values calculated from electrochemical measurements with H_2O_2 used as a hole scavenger (Fig. S6†). While H-Al and H-Zr showed a particular improvement for $\eta_{sep.}$, the dual-modified photoanode showed a synergistic effect that goes beyond the simple summation of the individual contributions, with a remarkable enhancement of catalytic efficiency. As the reduction of polaronic effects hypothesized for Al^{3+} lattice doping only improves intragrain electronic mobility (*i.e.*, within the crystal lattice), these findings corroborate the slightly higher overall efficiency of H-0.5Al when compared to pristine hematite (H). The attributed segregation of Zr^{4+} at the interfaces, on the other hand, can address the bottleneck of bulk electronic conductivity by efficiently decreasing the Schottky energy barriers at the grain boundaries,[42] therefore allowing electron hopping through hematite grains and consequently enhancing its overall efficiency more prominently.

To elucidate the effect of Zr^{4+} incorporation when it segregates at the grain boundary, density functional theory (DFT) calculations were performed using a grain boundary (GB) model with 25° between grains (Fig. 3a), following the procedure proposed in the previous report.[42] The chemical substitution of Fe^{3+} by Zr^{4+} at the GB promotes a reduction of the effective electron potential energy barrier (Fig. 3b) that can be understood by the lower potential energy $\left(Z_{eff}\frac{e}{r}\right)$ of the higher effective atomic number (Z_{eff}) of Zr. A quantitative estimation of the impact of this lower potential energy barrier on the electron transport across the GB was done by approximating to a quantum tunnelling problem of a rectangular barrier potential profile. Herein, the barrier width is $a = 2.5$ Å, and the height decreases from $V_0 = 1.88$ in pure hematite to $V_1 = 1.48$ eV upon Zr segregation, relative to the bulk mean potential ($\overline{v_b}$). The electron transmission was calculated and increases upon Zr doping by ~3 times for lower electron kinetic energies $E < V_1$ and ~1.5 times for higher electron kinetic energies $E > V_0$ (for

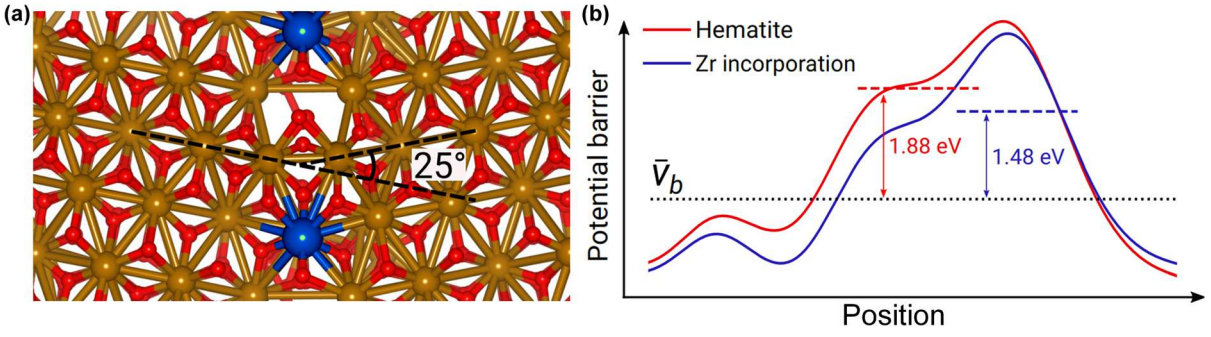

Fig. 3 Potential barrier effect of Zr^{4+} incorporation on the grain boundary. (a) Grain boundary model with 25° between grains, calculated with density functional theory (DFT). The Fe, O, and Zr atoms are shown in gold, red, and blue. (b) The effective average potential across the grain boundary, given by the sum of the contributions from the ionic potentials and the electronic Hartree and exchange-correlation potentials. The horizontal axis corresponds to the horizontal direction in (a).

details, see the Theory section and Fig. S7 from the ESI File†). The conductivity for a polycrystalline material with non-percolating grain transport depends directly on the tunnelling rate between grains. As such, the photocurrent density will be proportional to the transmission rate of the electrons between grains, making this microscopic model an effective interpretation for the segregation effects, as already shown for Sn^{4+} incorporation.[42]

Intensity modulated photocurrent spectroscopy (IMPS) was applied as a frequency-resolved optoelectronic characterization technique to give further insights on the charge carrier dynamics mechanism during simulated PEC operation, as shown in Fig. 4.

The low frequency semicircles (first quadrant) of IMPS plots can be used to determine the transfer and recombination rate constants that may depend on the applied potential (Fig. S8†).[43] The presence of pronounced semicircles in the first quadrant for pristine hematite (Fig. S9†) and H-Al (Fig. 4e) indicates that surface processes strongly affect the photoanode efficiency.[44] The model employed in this analysis considers that, at potentials where hole transfer is slow, holes tend to accumulate in traps at the surface, creating a competition between charge transfer and surface recombination.[44] A slight overall enhancement of charge separation and transfer efficiencies was observed for H-Al (Fig. 4i and m) throughout the potential range analyzed. This could be attributed to the reduction of polaronic effects at the hematite grains, promoted by a symmetry change of the Fe^{3+} chemical environment upon Al^{3+} addition. The enhancement of charge transport is limited, though, because the bottleneck of planar hematite conductivity is the high energy barriers at the grain boundaries.[42]

Conversely, the IMPS plots of H-Zr and H-Al–Zr display a charge transfer enhancement at potentials more positive than 1.2 V since the first quadrant loops disappeared. This result shows that Zr^{4+} is most likely segregating at hematite grain–grain interfaces, hence lowering the energy barrier height at the grain boundaries and allowing improved charge transport. Although a shift in the charge transfer efficiency (Fig. 4n) is noticeable after Zr^{4+} addition, it seems that the simultaneous modification with Al^{3+} and Zr^{4+} minimizes that voltage loss, thus achieving the maximal charge transfer efficiency with a smaller overpotential when compared to H-Zr (Fig. 4o). Interestingly, charge separation

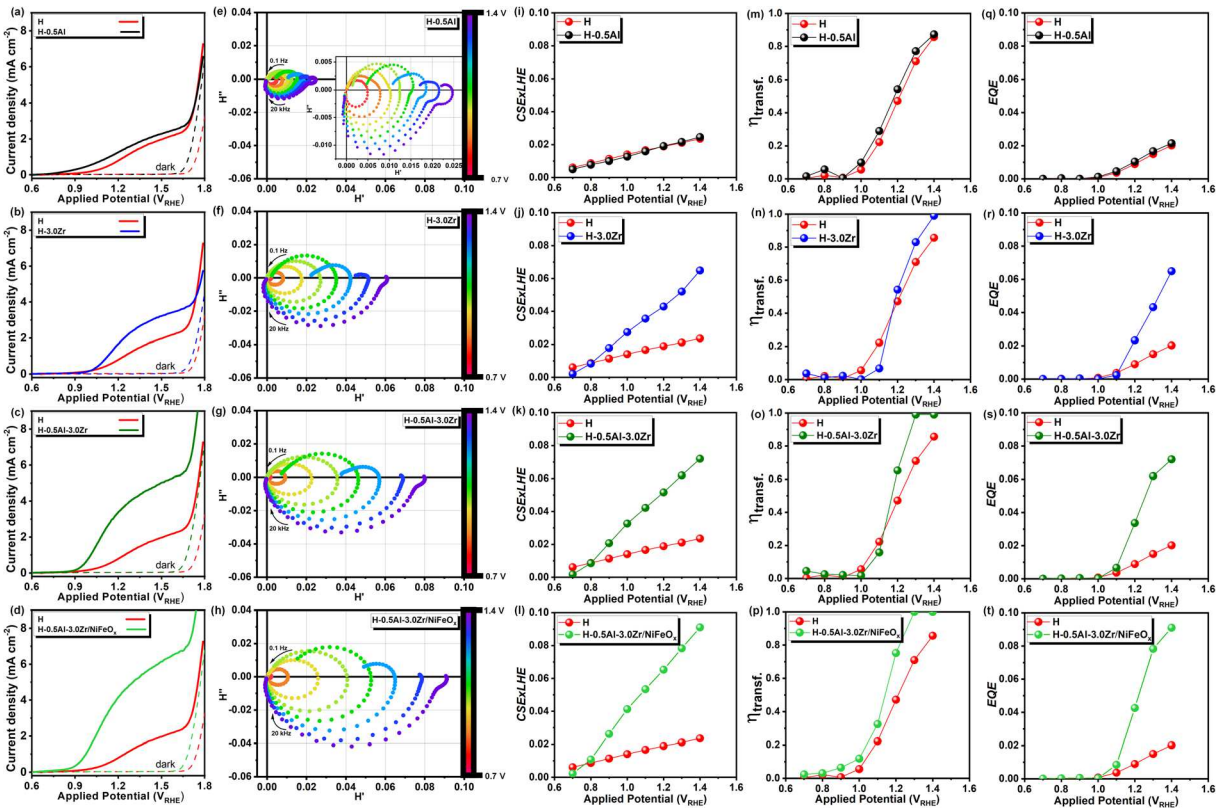

Fig. 4 (a–d) Linear voltammetry photocurrent density profiles of H-0.5Al, H-3.0Zr, H-0.5Al–3.0Zr, and H-0.5Al–3.0Zr/$NiFeO_x$, respectively, compared to pristine hematite (H) under AM 1.5G 100 mW cm^{-2} illumination in 1 M NaOH electrolyte. (e–h) Intensity modulated photocurrent spectroscopy (IMPS) plots of H-0.5Al, H-3.0Zr, H-0.5Al–3.0Zr, and H-0.5Al–3.0Zr/$NiFeO_x$, respectively, from 0.7 V to 1.4 V *vs.* RHE (step of 0.1 V), measured under 30 mW cm^{-2} monochromatic ($\lambda = 470$ nm) illumination in 1 M NaOH electrolyte. (i–l) Charge separation efficiency (CSE) values as a function of the light harvesting efficiency (LHE) calculated from the IMPS general theory of H-0.5Al, H-3.0Zr, H-0.5Al–3.0Zr, and H-0.5Al–3.0Zr/$NiFeO_x$, respectively, compared to pristine hematite (H). (m–p) Charge transfer efficiency ($\eta_{transf.}$) values calculated from the IMPS general theory of H-0.5Al, H-3.0Zr, H-0.5Al–3.0Zr, and H-0.5Al–3.0Zr/$NiFeO_x$, respectively, compared to pristine hematite (H). (q–t) External quantum efficiency (EQE) values calculated from the IMPS general theory of H-0.5Al, H-3.0Zr, H-0.5Al–3.0Zr, and H-0.5Al–3.0Zr/$NiFeO_x$, respectively, compared to pristine hematite (H).

efficiency (CSE) at 1.2 V for H-Al–Zr presents a 3-fold and 1.5-fold increase compared to pristine hematite or H-Al, and H-Zr, respectively. These results indicate the relevant synergistic effect of Al^{3+} and Zr^{4+} doping, while particularly indicating the benefits of designed Zr^{4+} segregation.

The addition of the $NiFeO_x$ co-catalyst improved the overall *j–V* curve of H-Al–Zr by showing a cathodic shift in the onset potential (Fig. S10†) and increasing the photocurrent response, suggesting that passivation of surface states occurred prior to charge transport enhancement.[45] The consequence is not only the minimization of the overpotential necessary for water oxidation (Fig. 4p), but also an increase in charge separation efficiency (Fig. 4l), which results in higher external quantum efficiency (EQE) values (Fig. 4t). Furthermore, the second semicircle observed in IMPS spectra at potentials $V > 1.2$ V has been detected in heterojunction systems, being associated with the RC^{-1} (time) constant, and presenting a similar rate to the transport constant.[46–48] Such behavior can be assumed considering the incorporation of modifiers in the hematite structure. A plausible hypothesis that can also be considered is that the electron mobility properties at the crystal interior and at the grain boundaries have been modified by Al^{3+} and Zr^{4+} incorporation, respectively, hence affecting the RC^{-1} (time) constant. In general, IMPS results show that, although charge carrier dynamics analysis can be a powerful tool to unveil the role of the dopants, a thorough microstructural analysis is also needed to objectively establish the photocurrent dependences on dopant distributions.

Transmission electron microscopy (TEM) coupled with energy-dispersive X-ray spectroscopy (EDS) was employed to further consolidate the evidence found about the Al^{3+} and Zr^{4+} roles (Fig. 5). From the analyzed representative region, it is possible to observe the FTO substrate at the bottom of the HAADF image with a brighter contrast and a fragment of the porous hematite nanostructure on top, where hematite grains are easily distinguishable. The image also highlights some hollow zones due to imperfect adherence on the substrate.

In addition, EDS analyses performed on the sample cross-sections revealed the elemental distribution across the microstructure induced by the PPS method. It is possible to verify that the Al^{3+} is uniformly spread across the grains, consistent with the formation of a solid solution as expected, considering its favorable enthalpy of mixing and the adopted synthetic method. Conversely, Mott–Schottky analysis showed a charge donor density of 4.87×10^{19} cm^{-3} for H and 8.53×10^{19} cm^{-3} for H-Al (Fig. S11 and Table S1†). This slight increase in charge donor density observed upon Al^{3+} addition is due to its same oxidation state as Fe^{3+}, with the increase being attributed to the more ionic behavior of Al^{3+}.

On the other hand, Zr^{4+} ions are segregated to regions that, when combined with the HAADF image, indicate an overlap with the grain boundaries, with some limited excess formation also at the surface regions. In agreement, the Mott–Schottky analysis of H-Zr showed a donor density of 1.14×10^{20} cm^{-3} (Fig. S11 and Table S1†), corroborating that the enhanced charge separation shown by IMPS analysis is due to the excess

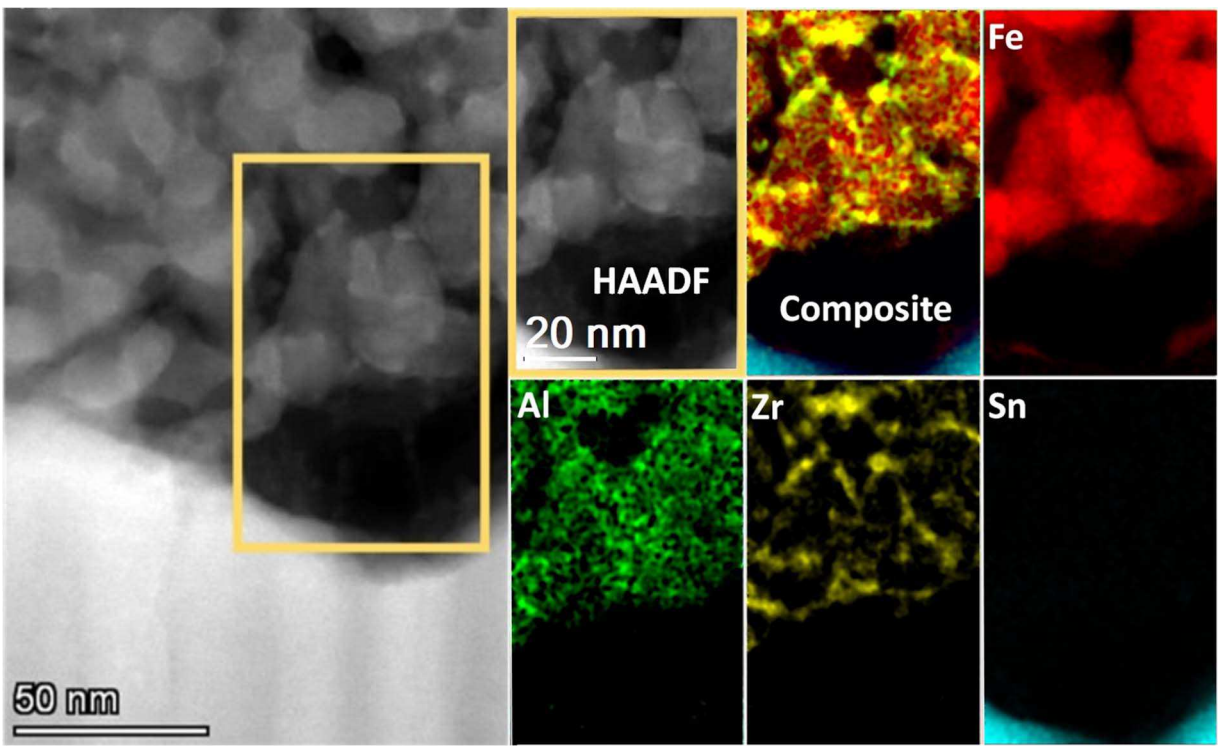

Fig. 5 High-resolution high-angle annular dark-field scanning transmission electron microscopy (HAADF-STEM) image of a cross-sectional H-Al–Zr photoanode with energy dispersive X-ray spectroscopy (EDS) analysis of a representative area of the lamella obtained by the focused ion beam (FIB) technique, showing the distribution of Fe^{3+}, Al^{3+}, Zr^{4+}, and Sn^{4+} elements.

Zr^{4+} content segregated at the interfaces. This demonstrates the effectiveness of PPS to induce the designed segregation, particularly at the grain–grain interfaces, with a possible cause-and-effect relationship with the observed photocurrent trends. Finally, one can see from Sn^{4+} EDS mapping that no significant amount of tin diffused to the photoabsorbing hematite layer, supporting negligible interferences from Sn^{4+} self-diffusion in the electrochemical measurements.[14]

X-ray photoelectron spectroscopy (XPS) analysis of the pristine hematite (H) photoanode shows Fe $2p_{1/2}$ (724.3 eV) and Fe $2p_{3/2}$ (710.7 eV) peaks characteristic of the α-Fe_2O_3 crystalline phase, confirming the presence of the trivalent oxidation state of iron (Fig. S12a†). The peaks attributed to the presence of Fe^{2+} species (Fe $2p_{1/2}$ at 722.9 eV and Fe $2p_{3/2}$ at 709.5 eV) are reasonable considering that annealing under an inert atmosphere (N_2 flux for 30 min) is most likely to change the surface chemistry of the photoanodes, either creating or removing defects which may cause the occurrence of Fe^{2+} species for charge compensation.[49] Indeed, in the O 1s spectra of pristine hematite (Fig. S12b†), while the most prominent peak (529.6 eV) is easily assigned to hematite lattice oxygen atoms (O_{latt}), the peak centered at 531.4 eV can be attributed to oxygen atoms in the vicinity of an oxygen vacancy or in the coordination sphere of a metal next to an oxygen vacancy.[50] This signal arises from the expected lack of core electrons to be emitted by an oxygen vacancy, as assigned (O_V). Moreover, the O 1s peak at 532.8 eV was assigned to superficially adsorbed –OH groups ($O_{ads.}$) for the hematite (H) sample.

There is a slight chemical shift of Fe 2p spectra to higher binding energies after doping regardless of its nature (Fig. S13a–d†). This behavior is expected for segregation, since the interfacial excess of ions would interfere in the Fe–O superficial bonds, consequently attracting the electron cloud of both Fe and O.[6] The similar behavior being observed for Al^{3+} doping could indicate that a local distortion caused by the different ionic radius might also change the chemistry of Fe^{3+} at the surface. However, XPS analysis is inconclusive for Al^{3+}, since EDS mapping showed that this dopant is most likely to form a solid solution at hematite bulk rather than forming excess at the surface. Chemical shifts to lower binding energies observed in O 1s spectra (Fig. S13e–h†) corroborate that the introduction of dopants gave a more ionic character to metal–oxygen bonds at the surface of the photoanodes.[29] Moreover, the Al 2p peaks at 73.4 eV for H-Al and H-Al–Zr photoanodes show the presence of Al^{3+} (Fig. S12c†), while Zr 3d spectra with doublet Zr $3d_{3/2}$ (181.6 eV) and Zr $3d_{5/2}$ (184.0 eV) shown in Fig. S12d† are consistent with fully oxidized Zr^{4+} in ZrO_2, as expected for materials annealed at high temperatures.[51]

A morphological evaluation of the photoanodes was done by scanning electron microscopy (SEM) (Fig. S14†). Top view images from SEM showed a classic "worm-like" planar morphology of spin-coating deposition solution methods.[9,52] SEM cross-section images further illustrate the planar morphology with stacked grains, and show the thicknesses of 174 nm for H, 271 nm for H-Al, 112 nm for H-Zr, and 248 nm for H-Al–Zr (Fig. S15†). This indicates that changes in porosity were induced by the different modifications introduced, delivering materials with different thicknesses, as the deposited mass remained constant following the PPS protocol. The evaluation of H-0.5Al–3.0Zr/$NiFeO_x$ surface composition and morphology after the 5 h operation shown in Fig. 2h revealed the maintenance of dopant amounts introduced to the photoanode (Fig. S16a–e and Table S2†) and undamaged surface morphology (Fig. S16f and g†). Besides the stable operation shown in Fig. 2h, the LSV experiment after testing (Fig. S16h†) revealed the same photocurrent density profile for H-0.5Al–3.0Zr/$NiFeO_x$, corroborating the potential of this material for stable technological applications.

Atomic force microscopy (AFM) (first row of Fig. 6) topography maps showed that the grain size of the H-Al sample is similar to that of pristine hematite (H), which is consistent with the assumption of lattice doping. However, the topography maps indicate that grain size seems to be considerably smaller for H-Zr. Ion segregation at the interfacial regions of oxide systems have been systematically correlated with grain size reduction.[53] This is because the interface energy decrease (either surface or grain boundary) associated with interfacial excess reduces the thermodynamic driving force for coarsening. This phenomenon is connected by the Gibbs adsorption isotherm to a local energy lowering[54] and allows greater stability of nanoparticles during synthesis or annealing protocols. Moreover, the grain size refinement due to ion segregation is commonly associated with a diminution of surface roughness since roughness is related somehow to adherence but mainly to the average grain sizes.[9] The electrochemical surface area (ECSA) obtained from cyclic voltammetry and calculated according to the procedure detailed in the ESI File (Fig. S17)† showed ECSA values of 5 (H), 6 (H-Al), 11 (H-Zr) and 18 (H-Al–Zr), corroborating the topographic characteristics observed by AFM.

From Kelvin probe force microscopy (KPFM) measurements, the surface potential distribution maps (second row of Fig. 6) display by high contrast a gradient accumulation of H and H-Al surface potential. Since both samples exhibit non-optimized interfaces, the electronic conductivity is not favored toward the bulk and therefore the electric current does not flow through the material. For H-Zr, the engineered grain–grain chemistry with Zr^{4+} allows electron hopping through the grain boundaries by lowering Schottky's energy barriers for charge conductivity. The result is a low contrast KPFM surface potential distribution map because the electric current flows readily through the material. The dual-modified photoanode presented a somewhat intermediate behavior when compared to H-Al and H-Zr samples, indicating that a superficial trade-off of charge distribution at the space charge layer might be responsible for the synergistic role of the dopants together. While H-Zr has improved photoelectrochemical performance in contrast to H-Al, one may speculate that, for H-Al–Zr, because Al^{3+} is dissolved in the hematite matrix, Zr^{4+} is further forced to segregate as the crystal lattice shrank due to the Fe^{3+} substitution to less electronegative ions. This would cause the dual-modified photoanodes to have a greater concentration of Zr^{4+} interfacial excess and, therefore, the most stable grains.

The capacitance gradient (dC/dz) maps displayed in the third row of Fig. 6 also corroborate the dopant distribution hypothesized by the PPS synthesis protocol. The higher contrast observed at the grain–grain interfaces of H and H-Al suggests that the grain boundaries act as charge recombination sites by accumulating and trapping charge carriers. Also noticeable is a reduction of contrast in the grains with the addition of Al^{3+} as a dopant, indicating that Al^{3+} is improving the conductivity within hematite grains by reducing polaronic effects due to Fe^{3+} electron effective mass.[55] Moreover, the H-Zr capacitance gradient map shows that the segregation of Zr^{4+} at the interfaces and its consequent grain size pinning mitigate the hematite grain boundary trapping effect. The combination of Al^{3+} and Zr^{4+} effects led the H-Al–Zr capacitance gradient map to exhibit low contrast grains compared to H-Zr. It also presented negligibly contrasted grain boundaries compared to H-Al, once again reinforcing the synergy of the dual modification designed by the PPS method.

Open circuit potential (OCP) measurements show higher ΔV OCP values for H and H-Al (Fig. S18b and Table S3†), indicating Al-doping does not significantly change the surface of the photoanodes. This corroborates that Al^{3+} is inside hematite grains rather than on the surface. Smaller ΔV OCP was found for H-Zr, indicating the creation of surface trapping states due to Zr^{4+} segregation at the surface. Normalized OCP values (Fig. S18c†) show fastest charge recombination for H, due to non-optimized interfaces. Smaller recombination rates were observed for H-Zr, indicating Zr^{4+} segregation at the grain boundaries optimizes the grain–grain interfaces, slowing down recombination. ΔV OCP values contrast with consistent ECSA growth with Al^{3+} and Zr^{4+} modifications. As Al^{3+} doping increases porosity (higher thickness) and Zr^{4+} segregation delivers smaller nanograins (thinner and more compact structure), a trade-off is observed between the morphology and surface electronic properties of the photoanodes on the active surface area values found.

Furthermore, electrochemical impedance spectroscopy (EIS) results support the trends observed in KPFM maps. Nyquist plots at 1.23 V_{RHE} under 100 mW cm^{-2} illumination (Fig. S19†) were fitted with the model circuit $[R_s(C_{bulk}R_{trapp})(CPE_{ss}R_{ss,ct})]$, where the electrolyte resistance is represented by R_s, (C_{bulk}-R_{trapp}) represents the hematite bulk capacitance and its charge trapping resistance, and ($CPE_{ss}R_{ss,ct}$) represents the surface capacitance and the resistance associated with charge carrier transfer from the bulk to the electrolyte in the presence of surface states. The CPE element was used due to the non-ideal dielectric behavior of the hematite solid–liquid interface in thin films.[56] The EIS fitting (Table S4†) showed the effectiveness of Al–Zr addition, improving hematite's charge transport properties. Fitted data shows a tendency of resistance drop ($R_{ss,ct}$) with the addition of each element, which means that H-Al–Zr/$NiFeO_x$ exhibited the lowest R_{trapp} and $R_{ss,ct}$ values of all photoanodes, justifying its best photoelectrochemical behavior.

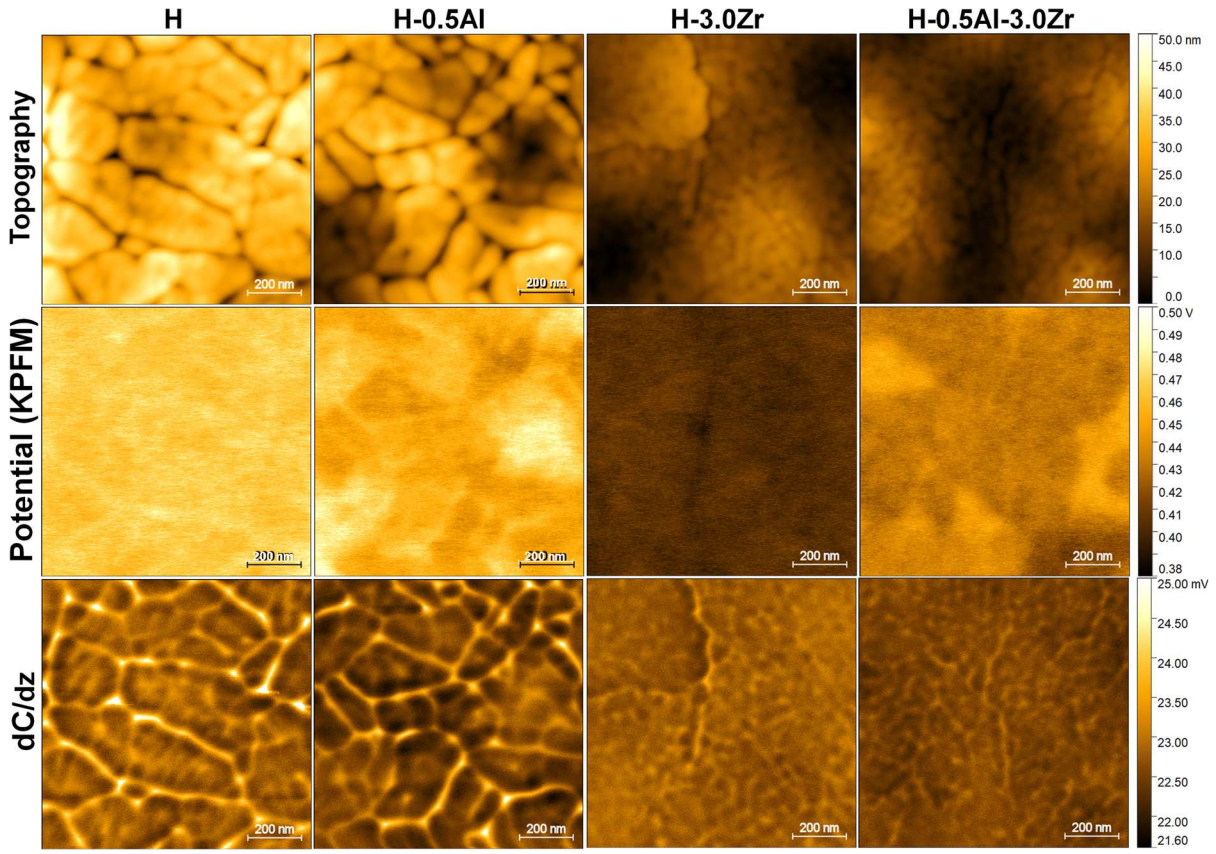

Fig. 6 Topography maps (first row), surface potential maps (second row), and capacitance gradient – dC/dz – maps (third row) of H, H-0.5Al, H-3.0Zr, and H-0.5Al–3.0Zr obtained by Kelvin probe force microscopy (KPFM).

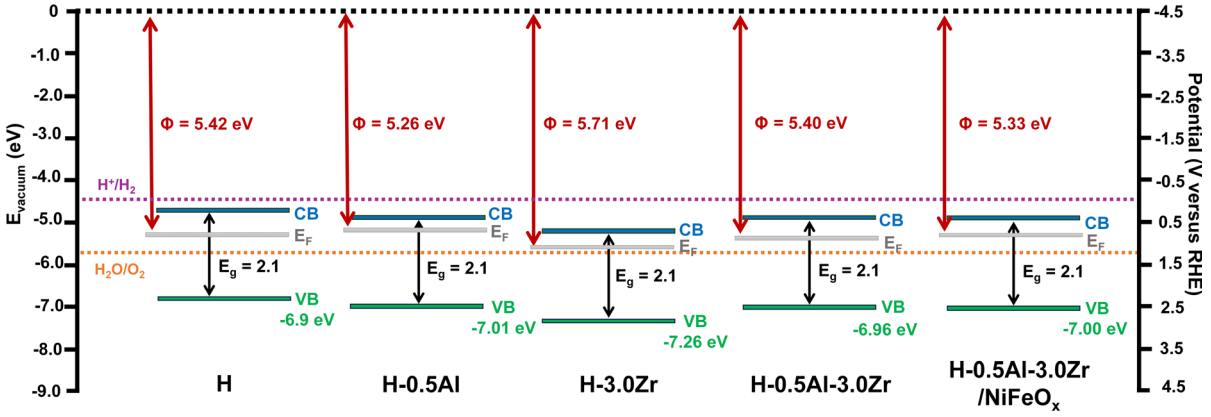

Fig. 7 Band diagrams obtained from ultraviolet photoelectron spectroscopy (UPS) spectra (Fig. S20†) of pristine hematite (H), H-0.5Al, H-3.0Zr, H-0.5Al–3.0Zr, and H-0.5Al–3.0Zr/NiFeO$_x$. Valence band (VB) maximum and work function (Φ) values of the semiconductors were extracted from the expansion of the region near the Fermi level and the determination of the secondary electron cutoff of the UPS spectra of the photoanodes. Gap energies (E_g) were extracted from Tauc plots (Fig. S21†).

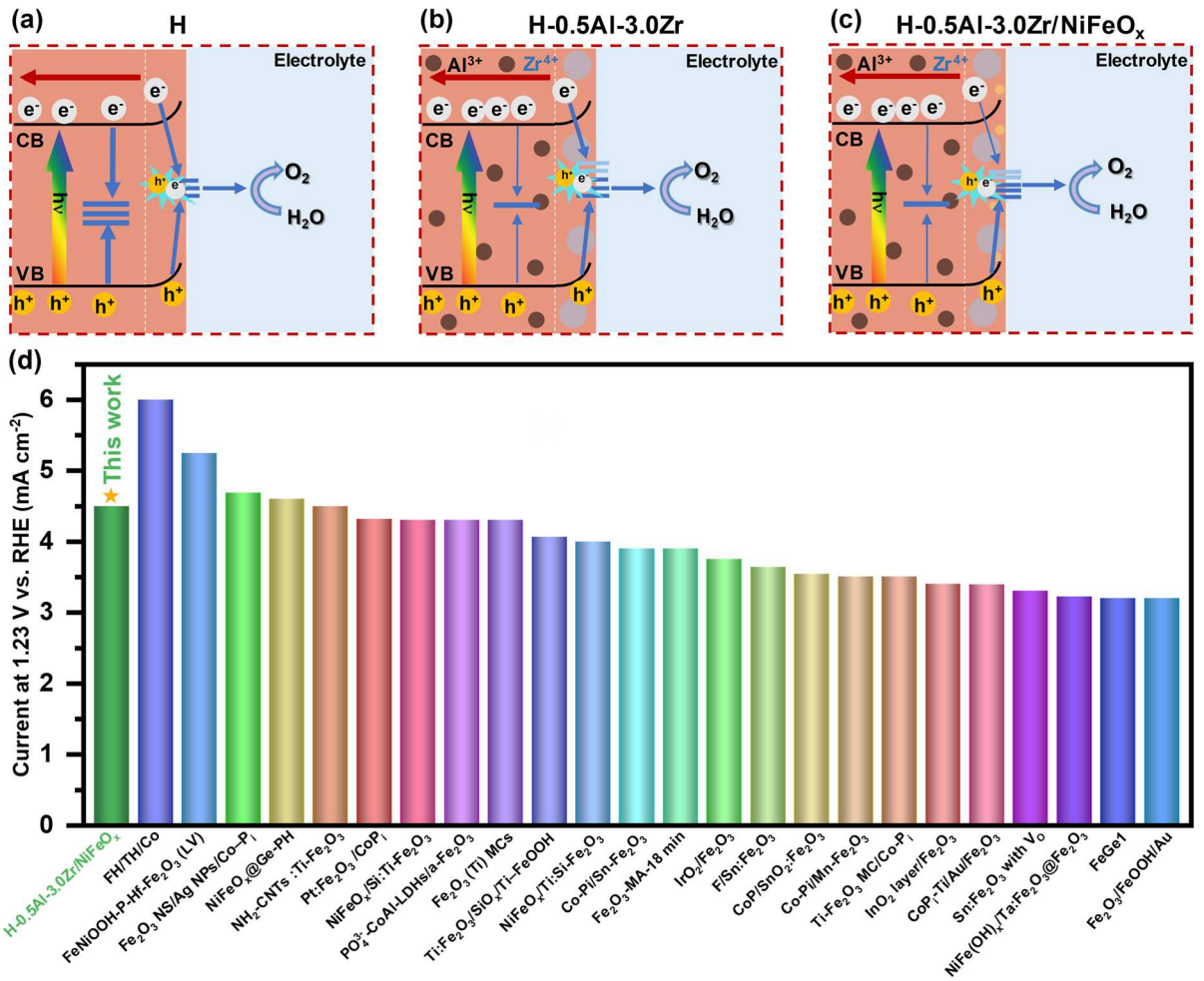

Fig. 8 (a) Schematic band diagram of pristine hematite photoelectrochemical (PEC) properties. The photoanode performance is strongly affected by bulk and surface recombination. (b) Schematic band diagram of H-0.5Al–3.0Zr PEC properties. The photoanode performance is enhanced by Al^{3+} lattice doping and Zr^{4+} segregation. (c) Schematic band diagram of H-0.5Al–3.0Zr/NiFeO$_x$ PEC properties. Besides Al^{3+} lattice doping and Zr^{4+} segregation, the addition of NiFeO$_x$ improves charge transport at the surface, mitigating defects caused by Zr^{4+} segregation at the surface. (d) Literature review of state-of-the-art hematite-based photoanodes compared to the water oxidation photocurrent obtained in this work (references for each sample mentioned can be found in the ESI File – Table S5†).

The ultraviolet photoelectron spectroscopy (UPS) electronic structure analysis of the photoanodes (Fig. S20†) exhibits the effects of dopant addition on the band diagrams of the semiconducting hematite-based photoanodes (Fig. 7). A pronounced shift of the Fermi level toward the conduction band (CB) is observed for Al^{3+} doping, corroborating that aluminum reduces polaronic effects since small polarons are mainly responsible for hematite Fermi level pinning.[57] H-3.0Zr exhibited a 0.66 eV energy difference from its CB position and the water reduction thermodynamic potential (−4.5 eV in E_{vacuum}), which was the largest value observed among the studied photoanodes. These results indicate the H-Zr requirement for a higher overpotential to drive the water oxidation reaction, consistent with the behavior previously observed in the IMPS charge transfer efficiency (Fig. 4n). Also, the more negative valence band (VB) position of H-Zr compared to H-Al shows the greater efficacy of Zr^{4+} segregation over Al^{3+} lattice doping on charge transport, also corroborating the trend observed for IMPS charge separation efficiencies in Fig. 4i and j. For H-Al–Zr/$NiFeO_x$, the trade-off of Al^{3+} and Zr^{4+} doping characteristics, associated with the co-catalyst behavior, led to a photoanode with reduced overpotential for water oxidation (0.4 eV from the CB to water reduction potential), with the Fermi level closer to the CB (thus favoring charge transfer efficiency), and the VB position more negative than for pristine hematite (indicating superior charge separation efficiency). Taken together, these findings and the performance of the photoanodes show the intricate relation between the band positioning of the semiconducting absorber materials and their photoelectrochemical behavior, once again corroborating the previous results and validating the hypothesis of selective doping with Al^{3+} and Zr^{4+} promoted by the polymeric precursor solution (PPS) method.

In summary, the selective modifications introduced onto hematite following the PPS protocol address three main drawbacks of α-Fe_2O_3: intragrain charge recombination, charge recombination at the grain boundaries, and recombination due to surface trapping states. As shown in Fig. 8a, charge carrier transport in pristine hematite is strongly affected by bulk and surface recombination. Fig. S22b† shows that Al^{3+} lattice doping (brown circles) cannot enhance the overall conductivity, but only reduces intragrain polaronic effects. When Zr^{4+} segregates at the interfaces (gray circles), as shown in Fig. S22c,† a trade-off between increased conductivity at the grain boundaries and the creation of more surface states is observed, resulting in enhanced charge separation efficiency. When both Al^{3+} and Zr^{4+} are incorporated (Fig. 8b), a synergistic effect is observed by aggregating the beneficial individual effects of the dopants. The addition of $NiFeO_x$ (small light-yellow circles) shown schematically in Fig. 8c further improves the photoelectrochemical performance of the photoanodes by passivating the surface states created by Zr^{4+} addition and therefore contributing to charge separation efficiency. The result of this rational engineering of hematite interfaces is a photoanode with state-of-the-art performance, as seen in Fig. 8d and Table S5.† The photoanode prepared by PPS showed a competitive photocurrent while employing earth-abundant chemical elements and can be easily adapted for the industrial scale.

4 Conclusions and outlook

Considering that one of the most significant bottlenecks in material synthesis is a selective control and modulation of properties by intentional structural modifications, the findings reported here demonstrate that the polymeric precursor solution (PPS) method is successful in delivering an effective dual-modification of hematite, inducing Al^{3+} to form a solid solution in the corundum structure, while Zr^{4+} segregated to the interfacial regions, particularly the grain boundaries of hematite. The designed elemental distribution strongly supports and explains the observed high photocurrents, with a clear synergistic impact of the dopants. Al^{3+} acts as a conventional crystal dopant, immersed in the lattice to reduce the polaronic effects. Because of its valence, Al^{3+} is not expected to increase the number of charge carriers but does impact charge mobility by mitigating small-polaron pinning effects. However, assuming a hopping mechanism for electron conduction, when doped with Al^{3+} alone, charges still face grain boundary energy barriers upon migration from one grain to another, limiting the overall photocurrent. Conversely, because Zr^{4+} is preferentially segregated to grain boundaries, it mostly impacts grain boundaries by locally satisfying broken chemical bonds and ion coordination. This grain boundary 'healing' effect decreases charge trapping by reducing the number of charge recombination sites. However, Zr^{4+} does nothing to impact polaronic effects, and it is only when put together with Al^{3+} that a synergistic effect allows for significantly improved photoelectrochemical performance. This rational design using the PPS method provides great perspectives in the development of green technologies exploiting earth abundant elements by selectively positioning them. The synergy observed upon Al^{3+}/Zr^{4+}/$NiFeO_x$ addition highlights the unprecedented positive impact in the overall photoelectrochemical performance achieved for hematite photoanodes with planar morphology, where high efficiencies were obtained with a cost-effective increase of photocurrent for water oxidation.

Author contributions

Nathália C. Verissimo: investigation, formal analysis, data curation, writing – review & editing. Fabio A. Pires: data curation, writing – original draft, writing – review & editing. Ingrid Rodríguez-Gutiérrez: formal analysis, data curation, writing – review & editing. Jefferson Bettini: formal TEM analysis. Tanna E. R. Fiuza: formal TEM analysis. Cleyton A. Biffe: formal AFM analysis. Fabiano E. Montoro: preparation of samples for TEM analysis. Gabriel R. Schleder: computational simulation analysis, writing – review & editing. Ricardo H. R. Castro: writing – original draft, research, writing – review & editing, visualization. Edson R. Leite: writing – review & editing. Flavio L. Souza: conceptualization, writing – review & editing, visualization, supervision, funding acquisition.

Conflicts of interest

There are no conflicts to declare.

Acknowledgements

The authors acknowledge CNPq, CAPES and FAPESP (Grants 2017/02317-2, 2021/10672-2, 2022/04150-6, and 2023/08273-8) funding. G. R. S. acknowledges support from CNPq – INCT (National Institute of Science and Technology on Materials Informatics, grant no. 371610/2023-0). N. C. V. and F. L. S. acknowledge FAPESP (Grant 2017/11986-5), Shell and the strategic importance of the support given by ANP (Brazil's National Oil, Natural Gas and Biofuels Agency) through the R&D levy regulation. R. H. R. C. acknowledges NSF DMR Ceramics 2015650.

References

1 W. Si, F. Haydous, U. Babic, D. Pergolesi and T. Lippert, *ACS Appl. Energy Mater.*, 2019, **2**, 5438–5445.
2 F. Li, J. Jian, Y. Xu, S. Wang, H. Wang and H. Wang, *Eng. Rep.*, 2021, **3**, 1–32.
3 D. Zhou and K. Fan, *Chin. J. Catal.*, 2021, **42**, 904–919.
4 T. H. Jeon, G. hee Moon, H. Park and W. Choi, *Nano Energy*, 2017, **39**, 211–218.
5 C. Lu, D. Zhang, Z. Wu, X. Zhao, K. Feng, G. Zhang, S. Wang, Z. Kang and J. Zhong, *Appl. Catal., B*, 2023, **331**, 122695.
6 K. T. Thomaz, K. C. Bedin, I. Rodríguez-Gutiérrez, N. C. Verissimo, J. Bettini and F. L. Souza, *Mater. Today Energy*, 2023, **37**, 101399.
7 D. N. Muche, T. M. dos Santos, G. P. Leite, M. A. Melo, R. V. Gonçalves and F. L. Souza, *Mater. Lett.*, 2019, **254**, 218–221.
8 D. N. Muche, S. A. Carminati, A. F. Nogueira and F. L. Souza, *Sol. Energy Mater. Sol. Cells*, 2020, **208**, 110377.
9 K. C. Bedin, B. Mouriño, I. Rodríguez-Gutiérrez, J. B. S. Junior, G. T. dos Santos, J. Bettini, C. A. R. Costa, L. Vayssieres and F. L. Souza, *Chin. J. Catal.*, 2022, **43**, 1247–1257.
10 J. B. Souza Junior, F. L. Souza, L. Vayssieres and O. K. Varghese, *Appl. Phys. Lett.*, 2021, **119**, 200501.
11 M. Chen, A. C. Grieder, T. J. Smart, K. Mayford, S. McNair, A. Pinongcos, S. Eisenberg, F. Bridges, Y. Li and Y. Ping, *Nanoscale*, 2022, **15**, 1619–1628.
12 T. J. Smart, V. U. Baltazar, M. Chen, B. Yao, K. Mayford, F. Bridges, Y. Li and Y. Ping, *Chem. Mater.*, 2021, **33**, 4390–4398.
13 H. J. Avila-Paredes and S. Kim, *Solid State Ionics*, 2006, **177**, 3075–3080.
14 F. A. Pires, G. T. dos Santos, J. Bettini, C. A. R. Costa, R. V. Gonçalves, R. H. R. Castro and F. L. Souza, *Sustainable Energy Fuels*, 2023, **7**, 5005–5017.
15 A. Subramanian, M. A. Mahadik, J. W. Park, I. K. Jeong, H. S. Chung, H. H. Lee, S. H. Choi, W. S. Chae and J. S. Jang, *Electrochim. Acta*, 2019, **319**, 444–455.
16 T. K. Sahu, A. K. Shah, A. Banik and M. Qureshi, *ACS Appl. Energy Mater.*, 2019, **2**, 4325–4334.
17 Q. Zhu, C. Yu and X. Zhang, *J. Energy Chem.*, 2019, **35**, 30–36.
18 J. Cai, H. Chen, C. Liu, S. Yin, H. Li, L. Xu, H. Liu and Q. Xie, *Dalton Trans.*, 2020, **49**, 11282–11289.
19 Z. Sun, G. Fang, J. Li, J. Mo, X. He, X. Wang and Z. Yu, *Chem. Phys. Lett.*, 2020, **754**, 137736.
20 K. Jeong, M. A. Mahadik, J. B. Hwang, W. S. Chae, S. H. Choi and J. S. Jang, *J. Colloid Interface Sci.*, 2021, **581**, 751–763.
21 T. Jiao, C. Lu, K. Feng, J. Deng, D. Long and J. Zhong, *J. Colloid Interface Sci.*, 2021, **585**, 660–667.
22 K. Kang, H. Zhang, J. H. Kim, W. J. Byun and J. S. Lee, *Nanoscale Adv.*, 2022, **4**, 1659–1667.
23 Kumar Dhandole, P. Anushkkaran, W. S. Chae, H. S. Chung, H. H. Lee, S. H. Choi, M. Cho and J. S. Jang, *Chem. Eng. J.*, 2022, **446**, 136957.
24 K. Dhandole, T. S. Koh, P. Anushkkaran, H. S. Chung, W. S. Chae, H. H. Lee, S. H. Choi, M. Cho and J. S. Jang, *Appl. Catal., B*, 2022, **315**, 121538.
25 Z. Zhong, G. Zhan, B. Du, X. Lu, Z. Qin and J. Xiao, *J. Colloid Interface Sci.*, 2023, **641**, 91–104.
26 P. Anushkkaran, M. A. Mahadik, W. S. Chae, H. Hwi Lee, S. Hee Choi and J. Suk Jang, *Appl. Surf. Sci.*, 2023, **623**, 157035.
27 B. Ramogayana, D. Santos-Carballal, K. P. Maenetja, N. H. De Leeuw and P. E. Ngoepe, *ACS Omega*, 2021, **6**, 29577–29587.
28 F. Kraushofer, Z. Jakub, M. Bichler, J. Hulva, P. Drmota, M. Weinold, M. Schmid, M. Setvin, U. Diebold, P. Blaha and G. S. Parkinson, *J. Phys. Chem. C*, 2018, **122**, 1657–1669.
29 W. G. Guimarães, G. F. de Lima and H. A. Duarte, *Hydrometallurgy*, 2023, **221**, 106125.
30 R. Rivera, H. P. Pinto, A. Stashans and L. Piedra, *Phys. Scr.*, 2012, **85**, 015602.
31 A. Kleiman-Shwarsctein, M. N. Huda, A. Walsh, Y. Yan, G. D. Stuckyst, Y. S. Hu, M. M. Al-Jassim and E. W. McMland, *Chem. Mater.*, 2010, **22**, 510–517.
32 J. C. Launay and G. Horowitz, *J. Cryst. Growth*, 1982, **57**, 118–124.
33 J. Simfukwe, R. E. Mapasha, A. Braun and M. Diale, *Catalysts*, 2021, **11**, 940.
34 H. Pan, X. Meng, D. Liu, S. Li and G. Qin, *Phys. Chem. Chem. Phys.*, 2015, **17**, 22179–22186.
35 J. P. Buban, T. Mizoguchi, N. Shibata, E. Abe, T. Yamamoto and Y. Ikuhara, *J. Ceram. Soc. Jpn.*, 2011, **119**, 840–844.
36 R. H. Castro, S. V. Ushakov, L. Gengembre, D. Gouvêa and A. Navrotsky, *Chem. Mater.*, 2006, **18**, 1867–1872.
37 K. C. Bedin, D. N. Muche, M. A. Melo, A. L. Freitas, R. V. Gonçalves and F. L. Souza, *ChemCatChem*, 2020, **12**, 3156–3169.
38 J. Li, S. K. Cushing, P. Zheng, F. Meng, D. Chu and N. Wu, *Nat. Commun.*, 2013, **4**, 2651.
39 M. Fondell, T. J. Jacobsson, M. Bomana and T. Edvinsson, *J. Mater. Chem. A*, 2014, **2**, 3352–3363.
40 F. Njoka, S. Mori, S. Ookawara and M. Ahmed, *Int. J. Hydrogen Energy*, 2019, **44**, 10286–10300.
41 P. Dias, A. Vilanova, T. Lopes, L. Andrade and A. Mendes, *Nano Energy*, 2016, **23**, 70–79.
42 F. C. De Lima, G. R. Schleder, J. B. Souza Junior, F. L. Souza, F. B. Destro, R. H. Miwa, E. R. Leite and A. Fazzio, *Appl. Phys. Lett.*, 2021, **118**, 201602.

43 E. A. Ponomarev and L. M. Peter, *J. Electroanal. Chem.*, 1995, **396**, 219–226.
44 Y. Dai, G. Xie, X. Jia, B. Guo and J. R. Gong, *Appl. Surf. Sci.*, 2023, **610**, 155501.
45 L. Freitas, D. N. Muche, E. R. Leite and F. L. Souza, *J. Am. Ceram. Soc.*, 2020, **103**, 6833–6846.
46 L. M. Peter, K. G. U. Wijayantha and A. A. Tahir, *Faraday Discuss.*, 2012, **155**, 309–332.
47 J. Su, L. Guo, N. Bao and C. A. Grimes, *Nano Lett.*, 2011, **11**(5), 1928–1933.
48 I. Rodríguez-Gutiérrez, E. Djatoubai, J. Su, A. Vega-Poot, G. Rodríguez-Gattorno, F. L. Souza and G. Oskam, *Sol. Energy Mater. Sol. Cells*, 2020, **208**, 110378.
49 J. Zhang and S. Eslava, *Sustainable Energy Fuels*, 2019, **3**, 1351–1364.
50 T. J. Frankcombe and Y. Liu, *Chem. Mater.*, 2023, **35**, 5468–5474.
51 C. Li, A. Li, Z. Luo, J. Zhang, X. Chang, Z. Huang, T. Wang and J. Gong, *Angew. Chem., Int. Ed.*, 2017, **56**, 4150.
52 K. Sivula, R. Zboril, F. Le Formal, R. Robert, A. Weidenkaff, J. Tucek, J. Frydrych and M. Grätzel, *J. Am. Chem. Soc.*, 2010, **132**, 7436–7444.
53 R. H. Castro, *Mater. Lett.*, 2013, **96**, 45–56.
54 H. Li, S. Dey and R. H. Castro, *Acta Mater.*, 2018, **150**, 394–402.
55 J. Bosman and H. J. van Daal, *Adv. Phys.*, 1970, **19**, 1–117.
56 R. Shoar Abouzari, F. Berkemeier, G. Schmitz and D. Wilmer, *Solid State Ionics*, 2009, **180**, 922–927.
57 A. Lohaus, A. Klein and W. Jaegermann, *Nat. Commun.*, 2018, **9**, 1–7.